POLITECNICO DI TORINO
Repository ISTITUZIONALE

Evaluation of the effective thermal conductivity of the unmelted powder particles during the electron beam powder bed fusion (EB-PBF) process

Original
Evaluation of the effective thermal conductivity of the unmelted powder particles during the electron beam powder bed fusion (EB-PBF) process / Rizza, G., Galati, M., Iuliano, L.. - ELETTRONICO. - 118:(2023), pp. 765-770. (16th CIRP Conference on Intelligent Computation in Manufacturing Engineering, CIRP ICME '22, Italy Ischia 13-15 Luglio 2022) [10.1016/j.procir.2023.06.131].

Availability:
This version is available at: 11583/2980970 since: 2023-08-06T15:28:45Z

Publisher:
Elsevier

Published
DOI:10.1016/j.procir.2023.06.131

Terms of use:

This article is made available under terms and conditions as specified in the corresponding bibliographic description in the repository

Publisher copyright

(Article begins on next page)

28 November 2026

Available online at www.sciencedirect.com

ScienceDirect

Procedia CIRP 118 (2023) 765–770

www.elsevier.com/locate/procedia

16th CIRP Conference on Intelligent Computation in Manufacturing Engineering, CIRP ICME '22, Italy

Evaluation of the effective thermal conductivity of the unmelted powder particles during the electron beam powder bed fusion (EB-PBF) process

Giovanni Rizza[a,*], Manuela Galati[a], Luca Iuliano[a]

[a]*Department of Management and Production Engineering (DIGEP), Integrated Additive Manufacturing center (IAM@PoliTo), Politecnico di Torino, Corso Duca degli Abruzzi 24, 10129 Torino, Italy*

* Corresponding author. Tel.: +39 0110907280; *E-mail address:* giovanni.rizza@polito.it

Abstract

The thermal conductivity of the unmelted powder particles in an electron beam powder bed fusion (EB-PBF) process is mainly determined by its sintering degree. A proper thermal conductivity is required to dissipate the heat generated during the melting and improve the beam matter interaction. In this work, the thermal conductivity is evaluated by image-based methodologies and thermal diffusion simulations. The effective neck growth and dimension are numerically calculated using phase field sintering simulations. The proposed methodology is able to provide crucial insight for the process optimisation without performing any experiment.

© 2023 The Authors. Published by Elsevier B.V.
This is an open access article under the CC BY-NC-ND license (https://creativecommons.org/licenses/by-nc-nd/4.0)
Peer-review under responsibility of the scientific committee of the 16th CIRP Conference on Intelligent Computation in Manufacturing Engineering

Keywords: Electron beam melting (EBM); Phase field; Ti6Al4V; Sintering

1. Introduction

In powder bed fusion Additive Manufacturing (AM) processes, the production is conducted by adding thin layers of metal powder particles and selectively melting the cross sections of the components. The characteristic that distinguishes the electron beam powder bed fusion (EB-PBF) process from the other AM processes is the use of an electron beam as an energy source. The electron beam works in a vacuum environment and allows high working temperatures. The vacuum environment is required to prevent deviation of the electron beam from the air molecules and ensure a high-quality beam [1]. The hot environment is required to prevent the "smoke" phenomena [2], which consists of a violent expulsion of powder particles from the powder bed [3]. Among the causes of "smoke" [3], the momentum transferred by the electron beam and the accumulation of negative charges on the surface of the powder particles were identified as the most difficult to overcome [4]. The first and the most adopted approach to prevent smoke was the introduction of the preheating step to increase the powder bed temperature. The high temperature produces a partial sinter of the powder particles, detectable as a neck [3,5]. Fig. 1 shows an example of powder particles partially sintered during the EB-PBF process. In this figure, the powder particles have diameters of 48.43 µm and 53.89 µm. These were maintained at a temperature around 923 K for approximately 1000 s. A neck diameter of 8.67 µm was found between the two powder particles.

The formation of the necks depends on the thermal history during the process. The temperature of the powder bed vary widely in the EB-PBF process [6]. Powder particles are relatively cold when raked on the build area [7]. Their temperature increase due to heat transmission from material below, that on the contrary is maintained at a high working temperature [8]. The temperature of the powder layer is further increased during the preheating step of the process, up to 50% - 70 % of the melting temperature of the material [9]. After preheating, the portion of the powder bed corresponding to the cross section of the components is melted. On the contrary, the remaining part of the powder bed see a cooling to the working temperature.

2212-8271 © 2023 The Authors. Published by Elsevier B.V.
This is an open access article under the CC BY-NC-ND license (https://creativecommons.org/licenses/by-nc-nd/4.0)
Peer-review under responsibility of the scientific committee of the 16th CIRP Conference on Intelligent Computation in Manufacturing Engineering
10.1016/j.procir.2023.06.131

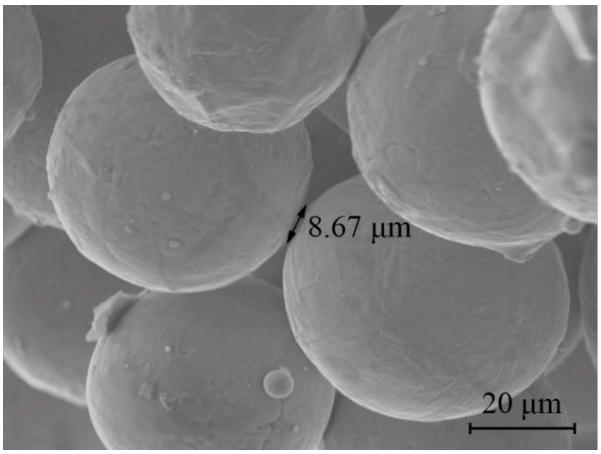


Fig. 1. Example of sintered powder particles obtained after the EB-PBF process.

This thermal history influences the dimension of the neck, which should be fine-tuned. Small necks could not guarantee adequate electrical and thermal conductivity among the particles, consequently carrying on the process safely [10]. The proper thermal conductivity is required to dissipate the heat generated during the melting and prevent part distortion [10]. Furthermore, the reduced thermal conductivity of the powder material, compared to bulk material, has proven to influence energy absorption and melting efficiency [11].

The problem of conductivity in powder material has been investigated for centuries. One of the first numerical models was proposed by Maxwell [12]. However, this model is difficult to apply to powder material because it neglects the contact area between particles and the difference between the thermal conductivity of the solid material and the gas [13]. Yagi and Kunii [14] proposed a theoretical model that considers the packing density and the shape of the particles of the powder bed. This model considers the thermal conduction through the bulk material, the contact point of the particles and the radiation phenomena through the surfaces of the powder particles. On the contrary, it neglects the thermal conductivity owed to the convection phenomena. A comparison between this theoretical model and the experimental data shows a good agreement. Hadley [15] proposed a formulation of thermal conductivity limited to a mixing parameter directly dependent on the powder density and the volume of void present in the sample. These powder characteristics were determined experimentally. Butt [16] proposed a model to evaluate the thermal conductivity of porous media in the presence of gas. The mechanisms identified were solid conduction and convection. The radiation term was neglected. Sih and Barlow [17] proposed a comprehensive model that considered the conduction within the solid material and through the contact points, the conduction through convection of the gas filling the pores and the radiation. The model keeps in account also the effective shape of the powder particles and the effective contact area between the powder particles.

All these models agreed in describing the thermal conductivity of powder material using three contributions: conduction within the solid material and through the neck of the sintered powder particles, convection of the gas in the pores and radiation phenomena through the pores. In the case of a vacuum environment, the convection mechanism can be neglected. In this case, the thermal conductivity (λ) is expressed according to Equation 1 [18]:

$$\lambda = \lambda_r + \lambda_c \quad (1)$$

where λ_r represents the contribution of the radiation phenomena and λ_c represents the contribution of the conduction phenomena. When the radiation conductivity is negligible [14–16], λ can be evaluated as a fraction of that of the solid material, scaled according to the neck dimension [18].

The thermal conductivity in powder bed fusion AM processes was investigated in different studies experimentally. Wei et al. [19] adopted the transient hot wire method to obtain the thermal conductivity of powder for the laser powder bed fusion (L-PBF) process. The experimental results obtained were compared to the results of the numerical model proposed by Butt [16]. The experimental results were in good agreement with the numerical counterparts. Zhang et al. [20] produced a hollowed sample to investigate the density and thermal conductivity of the powder material processed with the L-PBF technique. The experimental results were combined with the information provided by a finite element (FE) model. With this methodology, the powder thermal conductivity of Ti6Al4V was found to vary from 3.4% to 5.2% of the solid material. Grose et al. [21] investigated the thermal conductivity of the powder bed of the micro selective laser sintering process using a simulation approach. For this scope, steady state FE thermal simulations were performed considering the effective arrangement of the nano powder particles at different sintering steps. Information about the arrangement of the powder particles was obtained from phase field (PF) simulations.

The approaches and the results obtained for the L-PBF process are not applicable to the EB-PBF process, because of different boundary conditions [22]. Modelling the thermal conductivity of sintered powder in a continuum FE model for EB-PBF process, Shen and Chou [23] and Galati et al. [24] assumed a body-centred packing structure and a constant neck radius between the powder particles. Gong et al. [25] investigated the thermal conductivity of sintered Ti6Al4V powder after the EB-PBF process. Thermal conductivity was evaluated using a thermal analyzer. The samples consisted of solid cylinders and hollowed open cylinders with sintered powder. The thermal conductivity was evaluated at different temperatures. Neira Arce [6] used the laser flash method to identify the thermal conductivity of powder material at different temperatures. A partial sinter of the initially loose powder was obtained when performing the measures at high temperatures. Smith et al. [10] investigated the thermal conductivity of the powder bed of the EB-PBF process by producing square hollowed samples that contain powder material sintered using different preheating parameter combinations. The laser flash method was adopted to measure the thermal conductivity at 40 °C and 730 °C. Leung et al. [26] investigated the effect of preheating parameters in EB-PBF process on the thermal conductivity of sintered Ti6Al4V powder. Cylindrical hollowed samples filled with only preheated sintered powder were produced directly attached to the start plate. These samples were extracted and characterized using micro-tomography. The thermal conductivity was evaluated by adopting image-based

methodologies. The results showed a small influence of the preheating parameters.

The current study investigates the effective thermal conductivity of the powder bed, considering the actual thermal history of the EB-PBF process. Phase field simulations were conducted to investigate the evolution of the neck formation between particles. An initial phase field simulation investigated the influence of the temperature history on the neck radius between powder particles. Another simulation considered powder particles with a granulometry typical for the EB-PBF process. The results of this phase field simulation were used to estimate the thermal conductivity. An image-based approach was adopted to evaluate this property at different stages, keeping in account the different sintering conditions.

Methodology

The convection thermal conductivity is negligible in the powder bed of the EB-PBF process, due to the vacuum environment. Moreover, the radiation thermal conductivity was considered negligible in the current study. This is two to three orders of magnitude smaller than that of solid and powder thermal conductivity, respectively [11]. Equation 2 was adopted to evaluate the thermal conductivity of the powder bed.

$$\lambda_{eff} = \alpha_{eff} \rho c_p \quad (2)$$

In this equation, λ_{eff} is the thermal conductivity of the powder bed, α_{eff} is the thermal diffusivity of the powder bed, ρ is the density of the powder and c_p is the specific heat capacity of the powder. For the current work, c_p was assumed equivalent to that of the bulk Ti6Al4V and ρ is obtained by scaling the bulk material density according to the density of the powder bed.

The thermal diffusivity of the powder was evaluated according to Equation 3.

$$\alpha_{eff} = \alpha_0 \frac{\varepsilon}{\tau} \quad (3)$$

where α_0 is the thermal diffusivity of the bulk Ti6Al4v, ε is the fraction of solid material in the powder bed, and τ is the tortuosity factor. ε and τ can be evaluated using the image-based approach proposed by Cooper et al. [30] and TauFactor, an application developed to evaluate the reduction of diffusivity in porous media, such as a powder bed [30]. In TauFactor, ε is calculated as the fraction of pixels occupied by bulk material divided by the total number of pixels of the picture adopted for the evaluation. τ is calculated from simulations of diffusion in TauFactor and describes the reduction of diffusivity in the powder bed owed to its convolution.

Phase field (PF) simulations were conducted to obtain the sintering condition of the powder bed during preheating of the EB-PBF process. The PF simulations were implemented according to the works proposed by Wang [27] and by Biswas et al. [28]. The PF equations were implemented in multiphysics object oriented simulation environment (MOOSE) [29]. The thermal load was described by the non isothermal conditions reported in Equation 4, which describes the EB-PBF temperature history.

$$T(t) = \begin{cases} 845 + int\left(\frac{t}{0.38}\right) \cdot 17.12 & \forall\ 0 < t \leq 9.5 \\ 1273 - 5.82(t - 9.5) & \forall\ 9.5 < t \leq 60 \\ 973 & \forall\ t > 60 \end{cases} \quad (4)$$

Equation 4 was then implemented in a user code into the PF simulation. The temperature is updated at each simulation step and used to evaluate all the terms of the PF equation that depends on temperature.

The influence of the temperature variability was investigated by simulating the sintering of two spherical Ti6Al4V powder particles. The diameter of the particles was assumed to be the same and equal to 80 μm. A simulation domain of 170 μm x 90 μm was considered with an initial mesh dimension of 1 μm. An automatic refinement algorithm was adopted to reduce the mesh dimension at the particle interface. Quadratic elements with nine nodes (QUAD9) were adopted for the mesh. A simulation time of 7200 s was considered. The initial time step was set to 10^{-3} s and was adaptively changed according to the simulation stability. The maximum dimension of the time step was however limited to 10 s for stability reasons

The material properties adopted for these simulations are reported in Table 1. The grain boundary diffusion was considered equal to $D_{GB}=0.1 \cdot D_S$.

Table 1. Material properties of Ti6Al4V alloy adopted for the phase field simulations.

Property	Value	Unit	Reference
Grain boundary mobility (ϑ_{GB})	10^{-11}	$m^4 \cdot J^{-1} \cdot s^{-1}$	[31]
Grain boundary energy (γ_{GB})	0.81	$J \cdot m^{-2}$	[32]
Surface energy (γ_S)	2.1	$J \cdot m^{-2}$	[32]
Surface diffusion activation energy (Q_S)	$1.19 \cdot 10^{-19}$	J	[31]
Surface diffusion pre-exponential factor (D^0_S)	$9.33 \cdot 10^{-8}$	$m^2 \cdot s^{-1}$	[31]
Volume diffusion activation energy (Q_S)	$3.2 \cdot 10^{-19}$	J	[33]
Surface diffusion pre-exponential factor (D^0_S)	$2.92 \cdot 10^{-19}$	$m^2 \cdot s^{-1}$	[33]
Molar volume (Ω)	$4.05 \cdot 10^{-29}$	m^3	

The results of applying the thermal load described by Equation 4 were compared with a corresponding simulation performed at the constant temperature of 845 K.

The thermal conductivity of a sintered powder bed was calculated considering six particles representative of a portion of the powder bed. The sintering was simulated using the PF model and the results were used as input for TauFactor. The diameter of the powder particles was assumed to be in the range of the EB-PBF process (45 μm - 105 μm). A simulation domain equal to 300 μm × 175 μm and a mesh dimension of 1.33 μm were adopted for the simulation. A mesh refinement algorithm was adopted so that the particle interface is described by at least 4 elements. Four nodes quadratic elements (QUAD4) were adopted. The simulation was performed for 9.5 s corresponding to the only the preheating step. The temperature was increased according to Equation 5.

$$T(t) = \left\{845 + int\left(\frac{t}{0.38}\right) \cdot 17.12 \quad \forall\ 0 < t \leq 9.5 \right. \quad (5)$$

Thermal conductivity was evaluated at different time during the sintering which corresponded to different temperatures and neck size. In particular, 10 pictures of the process were

extracted. The images were cropped and thresholded so that only two phases are present in the pictures, considering as a threshold value for the solid material c=0.76. The effective powder thermal diffusivity was obtained from Equation 3, where the tortuosity factor and the porosity were automatically calculated using TauFactor. The diffusivity of the bulk Ti6Al4V alloy (α_0) was evaluated according to Equation 6.

$$\alpha_0 = \frac{\lambda_0}{\rho_0 C_p} \quad (6)$$

The bulk Ti6Al4V thermal conductivity (λ_0), the bulk Ti6Al4V density (ρ_0) and the bulk Ti6Al4V specific heat (c_p) were obtained from Ref.[34]. The density of the powder (ρ) (for Equation 2) was obtained by scaling the density of the bulk Ti6Al4V by a factor equal to ε.

Results and discussions

Fig. 2 compares the estimated neck radius from the simulation conducted at the constant temperature to that of the simulation conducted under non-isothermal conditions (Equation 4). While the neck radiuses were comparable at the end of the simulation time (13.92 µm), large differences can be detected at the beginning of the neck formation. After 60 s, at the end of the thermal cycle, the neck radius for the simulation conducted at constant temperature was found to be 6.80 µm. The corresponding counterpart under non-isothermal conditions was 9.43 µm, which is around 39% times larger. This proves the high influence of the thermal history on the neck radius. Moreover, smaller neck radiuses will presumably produce smaller thermal and electrical conductivity in the powder bed and affect the thermal distribution.

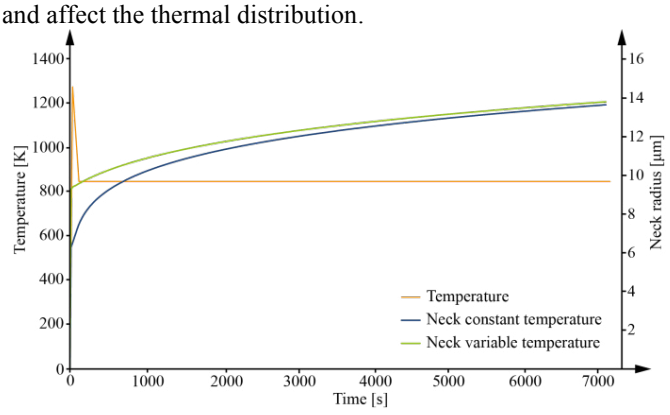


Fig. 2. Neck radius evolution, considering a constant or variable temperature. The temperature profile adopted for the simulation with variable temperature is also reported.

Fig. 3 reports an example of the picture adopted for the thermal conductivity evaluation. The white represents the bulk material, while the black represents the vacuum between the powder particles.

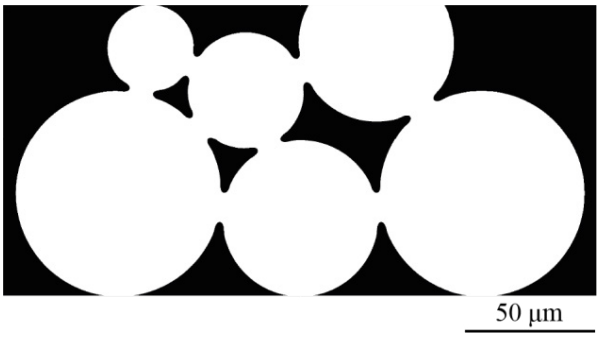


Fig. 3. Example of the cropped and thresholded image adopted for the thermal conductivity evaluation. The image is extracted from phase field simulations. The white represents the bulk material while the black represents the vacuum between the powder particles.

Table 2 reports the results of the thermal conductivity calculations. The mean neck diameter was also reported as the effective thermal conductivity depends on the temperature of the system and the neck area between the powder particles. The mean neck has been measured at different points of the thermal load (Equation 5). These data were adopted to calculate Equation 2, Equation 3, and Equation 6. As expected, the thermal conductivity increases with the temperature because of the increase in the neck size. The thermal conductivity of the powder bed was found to vary in a range between 1.40 W·m-1·K-1 at 0.5 s to 4.38 W·m-1·K-1 at 9.5 s.

Table 2. Thermal conductivity of Ti6Al4V powder bed (λ_{eff}) obtained from image-based simulations and the data adopted for its evaluation.

Time [s]	Temperature [K]	Mean neck [µm]	α_{eff} [$m^2 \cdot s^{-1}$]	λ_{eff} [$W \cdot m^{-1} \cdot K^{-1}$]
0.5	879	2.10	$5.30 \cdot 10^{-7}$	1.40
1.5	913	5.34	$6.64 \cdot 10^{-7}$	1.80
2.5	964	7.93	$1.06 \cdot 10^{-6}$	2.98
3.5	1016	10.78	$1.08 \cdot 10^{-6}$	3.15
4.5	1050	12.32	$1.16 \cdot 10^{-6}$	3.45
5.5	1101	13.32	$1.15 \cdot 10^{-6}$	3.53
6.5	1153	13.91	$1.17 \cdot 10^{-6}$	3.71
7.5	1187	14.74	$1.22 \cdot 10^{-6}$	3.94
8.5	1239	15.25	$1.97 \cdot 10^{-6}$	4.10
9.5	1273	16.42	$2.06 \cdot 10^{-6}$	4.38

Figure 4 shows graphically the variation of thermal conductivity in the powder bed with the temperature and compares the obtained data with the corresponding bulk material. A strong difference was found in the thermal conductivity values in the first two temperature steps, in which the neck grows rapidly. For the subsequent steps of the simulation, in which the neck growth rate is constant, the thermal conductivity varies linearly with the temperature. Therefore, it seems that two different trends can be detected for the thermal conductivity of the powder bed, in which the neck growth rate can play a determinant role. Another possible explanation for this difference could be the reduced neck dimension at the two initial temperature steps. The neck dimension may be more influential on thermal conductivity below a certain dimension. Above this dimension, temperature

of the system may become more influential than neck dimension. The thermal conductivity of the powder bed is an order of magnitude lower of the corresponding bulk material. When the neck growth rate becomes constant, the variation rate of the thermal conductivity of the powder bed became comparable to that of the bulk material.

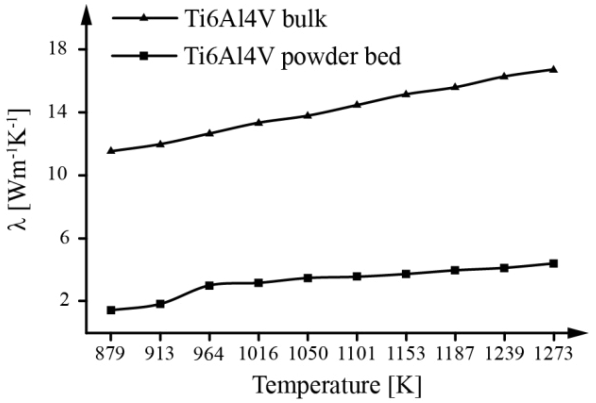


Fig. 4. Thermal conductivity of powder bed and bulk material at different temperatures.

Conclusions

For the EB-PBF process, a proper thermal conductivity for the unmelted sintered powder is required to conduct the process safely and ensure a good beam matter interaction. In this work, the influence of the sintering degree on the thermal conductivity of the powder bed has been investigated. The thermal conductivity of the powder bed has been evaluated with an image-based approach. PF simulations have been adopted to investigate the sintering conditions during the preheating step of the EB-PBF process.

The temperature history was found to strongly influence the neck dimension. Two PF simulations have been conducted considering isothermal and non isothermal conditions. Negligible differences have been identified between the neck radiuses at the end of the simulation time. On the contrary, Strong differences have been found at the beginning of the simulations. The neck radius was found to be larger for the non isothermal simulations than that obtained with simulations at a constant temperature. This difference assumes higher relevance considering the influence of the powder bed characteristics before the melting step.

To evaluate thermal conductivity, another PF sintering simulation has been conducted. For this simulation, six powder particles have been considered under the non isothermal conditions that characterize the preheating step. Ten images at different points of the thermal history were extracted. These pictures were adopted to evaluate the thermal conductivity of the powder bed with an image-based approach, using TauFactor.

The thermal conductivity of the first two temperature steps differs from that of the remaining thermal history. This difference may have been caused by the different neck growth rates of the initial simulation steps. This effect has been found less influential on the other time steps, where the neck growth ratio became constant. Another possible explanation for this difference in the first two steps, may be the presence of a boundary value for the neck dimension. Above this dimension, the temperature of the system become more influent on the thermal conductivity than the neck dimension. On the whole, the thermal conductivity of the powder bed was found to vary between 1.40 $W \cdot m^{-1} \cdot K^{-1}$ at 0.5 s to 4.38 $W \cdot m^{-1} \cdot K^{-1}$ at 9.5 s.

The approach presented in the current work has shown the capability to evaluate the thermal conductivity without using expensive experimental campaigns. This approach can easily be extended to other materials and other additive manufacturing techniques. In the case of the EB-PBF process, this approach may help to speed up the new material development and to gain a deeper knowledge of how to manage the process condition to conduct a safe process assuring a good beam matter interaction and finally a good quality of the produced components.

References

[1] Koike M, Martinez K, Guo L, Chahine G, Kovacevic R, Okabe T. Evaluation of titanium alloy fabricated using electron beam melting system for dental applications. J. Mater. Process. Technol. 2011 211 1400–1408.
[2] Cordero ZC, Meyer HM, Nandwana P, Dehoff RR. Powder bed charging during electron-beam additive manufacturing. Acta Mater. 2017 124 437–445.
[3] Milberg J, Sigl M. Electron beam sintering of metal powder. Prod. Eng. 2008 2 117–122.
[4] Galati M, Iuliano L. A literature review of powder-based electron beam melting focusing on numerical simulations. Addit. Manuf. 2018 19 1–20.
[5] Larsson M, Snis A. Method and device for producing three-dimensional objects, 06758093.6, 2008.
[6] Neira Arce A. Thermal Modeling and Simulation of Electron Beam Melting for Rapid Prototyping on Ti6Al4V Alloys, North Carolina State University, 2012. https://www.proquest.com/docview/1345924365/abstract/3E37C3575D824C4EPQ/1?accountid=28840.
[7] Shen N, Chou YK. Numerical thermal analysis in electron beam additive manufacturing with preheating effects, in: Proc. 23rd Solid Free. Fabr. Symp. Austin, TX, 2012: pp. 774–784.
[8] Shen N, Chou K. Numerical thermal analysis in electron beam additive manufacturing with preheating effects, in: 23rd Annu. Int. Solid Free. Fabr. Symp. - An Addit. Manuf. Conf. SFF 2012, 2012: pp. 774–784.
[9] Galati M, Defanti S, Saboori A, Rizza G, Tognoli E, Vincenzi N, Gatto A, Iuliano L. An investigation on the processing conditions of Ti-6Al-2Sn-4Zr-2Mo by electron beam powder bed fusion: Microstructure, defect distribution, mechanical properties and dimensional accuracy. Addit. Manuf. 2022 50 102564.
[10] Smith CJ, Tammas-Williams S, Hernandez-Nava E, Todd I. Tailoring the thermal conductivity of the powder bed in Electron Beam Melting (EBM) Additive Manufacturing. Sci. Rep. 2017 7 1–8.
[11] Zhao Y, Koizumi Y, Aoyagi K, Yamanaka K, Chiba A. Thermal properties of powder beds in energy absorption and heat transfer during additive manufacturing with electron beam. Powder Technol. 2021 381 44–54.
[12] Maxwell JC. A treatise on electricity and magnetism second ed. Clarendon Press, Oxford, 1881.
[13] Gusarov A V., Laoui T, Froyen L, Titov VI. Contact thermal conductivity of a powder bed in selective laser sintering. Int. J. Heat Mass Transf. 2003 46 1103–1109.
[14] Yagi S, Kunii D. Studies on effective thermal conductivities in packed beds. AIChE J. 1957 3 373–381.
[15] Hadley GR. Thermal conductivity of packed metal powders. Int. J. Heat Mass Transf. 1986 29 909–920.
[16] Butt JB. Thermal conductivity of porous catalysts. AIChE J. 1965 11 106–112.
[17] Sih SS, Barlow JW. Measurement and prediction of the thermal conductivity of powders at high temperatures. Solid Free. 400 Fabr. Symp. Proc. 1992 321–329.

[18] Tolochko NK, Arshinov MK, Gusarov A V., Titov VI, Laoui T, Froyen L. Mechanisms of selective laser sintering and heat transfer in Ti powder. Rapid Prototyp. J. 2003 9 314–326.
[19] Wei LC, Ehrlich LE, Powell-Palm MJ, Montgomery C, Beuth J, Malen JA. Thermal conductivity of metal powders for powder bed additive manufacturing. Addit. Manuf. 2018 21 201–208.
[20] Zhang S, Lane B, Whiting J, Chou K. On thermal properties of metallic powder in laser powder bed fusion additive manufacturing. J. Manuf. Process. 2019 47 382–392.
[21] Grose J, Cullinan M, Dibua OG, Behera D, Foong CS. Simulation and Characterization of Nanoparticle Thermal Conductivity for a Microscale Selective Laser Sintering System. Proc. ASME 2021 16th Int. Manuf. Sci. Eng. Conf. MSEC 2021. 2021 2.
[22] Shen N, Chou K. Thermal Modeling of Electron Beam Additive Manufacturing Process: Powder Sintering Effects. ASME 2012 Int. Manuf. Sci. Eng. Conf. Collocated with 40th North Am. Manuf. Res. Conf. Particip. with Int. Conf., MSEC 2012. 2013 287–295.
[23] Shen N, Chou K. Simulations of Thermo-Mechanical Characteristics in Electron Beam Additive Manufacturing. ASME Int. Mech. Eng. Congr. Expo. Proc. 2013 3 67–74.
[24] Galati M, Iuliano L, Salmi A, Atzeni E. Modelling energy source and powder properties for the development of a thermal FE model of the EBM additive manufacturing process. Addit. Manuf. 2017 14 49–59.
[25] Gong X, Cheng B, Price S, Chou K. Powder-bed electron-beam-melting additive manufacturing: powder characterization, process simulation and metrology. Early Career Tech. Conf. Birmingham, AL. 2013 55–66.
[26] Leung CLA, Tosi R, Muzangaza E, Nonni S, Withers PJ, Lee PD. Effect of preheating on the thermal, microstructural and mechanical properties of selective electron beam melted Ti-6Al-4V components. Mater. Des. 2019 174 107792.
[27] Wang YU. Computer modeling and simulation of solid-state sintering: A phase field approach. Acta Mater. 2006 54 953–961.
[28] Biswas S, Schwen D, Singh J, Tomar V. A study of the evolution of microstructure and consolidation kinetics during sintering using a phase field modeling based approach. Extrem. Mech. Lett. 2016 7 78–89.
[29] Permann CJ, Gaston DR, Andrš D, Carlsen RW, Kong F, Lindsay AD, Miller JM, Peterson JW, Slaughter AE, Stogner RH, Martineau RC. MOOSE: Enabling massively parallel multiphysics simulation. SoftwareX. 2020 11 100430.
[30] Cooper SJ, Bertei A, Shearing PR, Kilner JA, Brandon NP. TauFactor: An open-source application for calculating tortuosity factors from tomographic data. SoftwareX. 2016 5 203–210.
[31] Yan W, Ma W, Shen Y. Powder sintering mechanisms during the pre-heating procedure of electron beam additive manufacturing. Mater. Today Commun. 2020 25 101579.
[32] Roth TA, Suppayak P. The surface and grain boundary free energies of pure titanium and the titanium alloy Ti6Al4V. Mater. Sci. Eng. 1978 35 187–196.
[33] Nemat-Nasser S, Guo WG, Cheng JY. Mechanical properties and deformation mechanisms of a commercially pure titanium. Acta Mater. 1999 47 3705–3720.
[34] Yang J, Sun S, Brandt M, Yan W. Experimental investigation and 3D finite element prediction of the heat affected zone during laser assisted machining of Ti6Al4V alloy. J. Mater. Process. Technol. 2010 210 2215–2222.